INTERNATIONAL JOURNAL FOR NUMERICAL METHODS IN FLUIDS
Int. J. Numer. Meth. Fluids **28**: 95–112 (1998)

FINITE ELEMENT ANALYSIS OF TWO- AND THREE-DIMENSIONAL FLOWS AROUND SQUARE COLUMNS IN TANDEM ARRANGEMENT

KATSUYA EDAMOTO[a,]* AND MUTSUTO KAWAHARA[b]

[a] *Engineering Research Division, Kawada Industnes, 1-3-11, Takinogawa, Kita-ku, Tokyo 114, Japan*
[b] *Department of Civil Engineering, Chuo University, 1-13-27, Kasuga, Bunkyo-ku, Tokyo 112, Japan*

SUMMARY

Two- (2D) and three-dimensional (3D) finite element analyses for flow around two square columns in tandem arrangement were performed with various column spacings and Reynolds numbers. The computed values were compared with the wind-tunnel results in terms of the aerodynamic characteristics of the leeward column. In most 2D computations, strong vortices were formed behind the windward column, irrespective of widely changed Reynolds numbers. This was different from the experimental phenomena of equivalent spacing, so that the computed time-averaged pressure coefficients were not identical to the experimental values except when the distance between the two columns was adequately wide or narrow. On the other hand, in 3D computation, distinct differences in flow structures behind the column were observed between Reynolds numbers of 10^3 and 10^4 and the pressure coefficient in the 3D analysis with $Re = 10^4$ agreed well with the experimental value. Thus, the effectiveness of 3D computations and Reynolds number effects on the flow around two square columns have been confirmed. © 1998 John Wiley & Sons, Ltd.

KEY WORDS: square columns in tandem; finite element method; improved BTD; 3D computation; aerodynamic characteristics

1. INTRODUCTION

In the application of computational fluid dynamics (CFD) to practical design operations, the flow around structures in tandem arrangement is one of the most challenging model configurations. The flow around the adjacent bodies can be readily understood to be a complicated stream structure, and it would have different aerodynamic characteristics from those of isolated bodies. Until recently, the wind-tunnel test was considered to be the most reliable method to investigate such phenomena. However, considerable efforts must be made in order to be successful with the systematic studies using the wind-tunnel test; due to the complex flow structures and the increasing number of parameters (e.g. shapes, arrangements, flow condition, etc.). From such viewpoints, it is quite appropriate to explore some rational methods to estimate characteristics of the flow past structures in tandem, and CFD can be considered to be a countermeasure in the near future. Although several attempts [1–3] were made to solve this problem, there are still unclear points on the applicability of numerical simulations.

---

* Correspondence to: Engineering Research Division, Kawada Industries, 1-13-11, Takinogawa, Kita-ku, Tokyo 114, Japan.

CCC 0271–2091/98/110095–18$17.50

Received January 1997
Revised April 1997

In this paper, flow field characteristics around square columns in tandem were computed as the subject of a research topic. The fractional step (FS) finite element method [4,5] was applied to calculations at low Reynolds numbers, while the space–time formulation by the improved BTD (IBTD) method [6], a modified BTD [7–9] stabilization coupled with the Crank–Nicolson scheme, was adopted for high Reynolds numbers and 3D calculations. The aerodynamic coefficients and the surface pressure distributions of the leeward column were computed at various Reynolds numbers and with different column locations. The differences between 2D and 3D computations were clarified in terms of the aerodynamic coefficients and flow structures. Thus, the effects of Reynolds number and column arrangements, and difference in 2D and 3D flow structure around the columns, have been confirmed. Some topics on the application of CFD to tandem structures are also discussed.

2. PROBLEM FORMULATION

The governing equations are the continuity and the Navier–Stokes equations for an incompressible viscous fluid. In dimensionless form, these are

$$\nabla \cdot \boldsymbol{u} = 0 \tag{1}$$

and,

$$\frac{\partial \boldsymbol{u}}{\partial t} + \boldsymbol{u} \cdot \nabla \boldsymbol{u} + \nabla p - Re^{-1}\nabla^2 \boldsymbol{u} = \boldsymbol{f}, \tag{2}$$

where $\boldsymbol{u}$, p, t, Re and $\boldsymbol{f}$ represent the velocity vector, pressure, time, Reynolds number and body force, respectively, and the symbol ∇^2 represents the Laplacian operator. The time discretization forms of Equations (1) and (2) are defined as

$$\nabla \cdot \boldsymbol{u}^{n+1} = 0, \tag{3}$$

$$\frac{\boldsymbol{u}^{n+1} - \boldsymbol{u}^n}{\Delta t} + \boldsymbol{u}^n \cdot \nabla \boldsymbol{u}^n + \nabla p^{n+1} - Re^{-1}\nabla^2 \boldsymbol{u}^n = \boldsymbol{f}, \tag{4}$$

where Δt is the time increment and n represents the variables at time $n\Delta t$. Applying the FS procedure, the following pressure Poisson equation (PPE) is easily derived from Equations (3) and (4), namely

$$\nabla^2 p^{n+1} = \frac{1}{\Delta t}\nabla \boldsymbol{u}^n - \nabla\{\boldsymbol{u}^n \cdot \nabla \boldsymbol{u}^n - Re^{-1}\nabla^2 \boldsymbol{u}^n - \boldsymbol{f}\}. \tag{5}$$

In the FS method, the velocity $\boldsymbol{u}^{n+1}$ is predicted by solving p^{n+1} from Equation (5) and substituting it into Equation (4). The finite element spatial discretization for both (4) and (5) was performed using the same linear triangular elements in this study; which resulted in the system of linear equations for the pressure and velocity.

For high Reynolds number and 3D computation, the IBTD stabilization was adopted for the FS method. Applying the Crank–Nicolson technique to the time derivative term of Equation (2) leads to

$$\boldsymbol{u}^{n+1} = \boldsymbol{u}^n + \Delta t \frac{\partial \boldsymbol{u}^n}{\partial t} + \frac{\Delta t^2}{2}\frac{\partial^2 \boldsymbol{u}^{n+1/2}}{\partial^2 t} + \boldsymbol{O}(\Delta t^3), \tag{6}$$

where $\boldsymbol{u}^{n+1/2} = (\boldsymbol{u}^{n+1} + \boldsymbol{u}^n)/2$, and $\boldsymbol{O}$ denotes the truncation error. Introducing Equation (2) to the second-order time derivative of Equation (6) leads to

$$\frac{\partial \boldsymbol{u}^2}{\partial t} \simeq \boldsymbol{u}\cdot\nabla\{\boldsymbol{u}\cdot\nabla\boldsymbol{u} + \nabla p - Re^{-1}\nabla^2\boldsymbol{u} - \boldsymbol{f}\} - \frac{\partial}{\partial t}\{\nabla p - Re^{-1}\nabla^2\boldsymbol{u} - \boldsymbol{f}\}, \tag{7}$$

in which the convective velocity is assumed to be independent of time. The last term of Equation (7) is approximated as

$$\begin{aligned}&\frac{\partial}{\partial t}\{\nabla p^{n+1/2} - Re^{-1}\nabla^2\boldsymbol{u}^{n+1/2} - \boldsymbol{f}^{n+1/2}\}\\ &= \frac{1}{\Delta t}\{\nabla p^{n+1} - Re^{-1}\nabla^2\boldsymbol{u}^{n+1} - \boldsymbol{f}^{n+1}\} - \frac{1}{\Delta t}\{\nabla p^{n} - Re^{-1}\nabla^2\boldsymbol{u}^{n} - \boldsymbol{f}^{n}\} + \boldsymbol{O}(\Delta t).\end{aligned} \tag{8}$$

By introducing Equations (2), (7) and (8) into Equation (6), the time discretization form of Equation (2), using the IBTD, is

$$\begin{aligned}&\frac{\boldsymbol{u}^{n+1} - \boldsymbol{u}^n}{\Delta t} + \boldsymbol{u}^n\cdot\nabla\boldsymbol{u}^n + \nabla p^{n+1/2} - Re^{-1}\nabla^2\boldsymbol{u}^{n+1/2}\\ &- \frac{\Delta t}{2}\boldsymbol{u}^n\cdot\nabla\{\boldsymbol{u}^n\cdot\nabla\boldsymbol{u}^{n+1/2} + \nabla p^{n+1/2} - Re^{-1}\nabla^2\boldsymbol{u}^{n+1/2} - \boldsymbol{f}\} = \boldsymbol{f},\end{aligned} \tag{9}$$

where the unknown velocity $\boldsymbol{u}^{n+1}$, associated with the convective term, has been replaced by $\boldsymbol{u}^n$ in order to construct the linear symmetric matrix to be solved. The last term of the left-hand side of Equation (9), the IBTD term, will make the dissipative error smaller than that of the FS method. The spatial discretization of Equation (9) was performed using the isoparametric quadrilateral elements (bilinear in 2D and trilinear in 3D) for both pressure and velocity. With the implementation of Equation (9), a larger time increment can be chosen in contrast to the FS method. This will be advantageous for high Reynolds numbers and 3D computations.

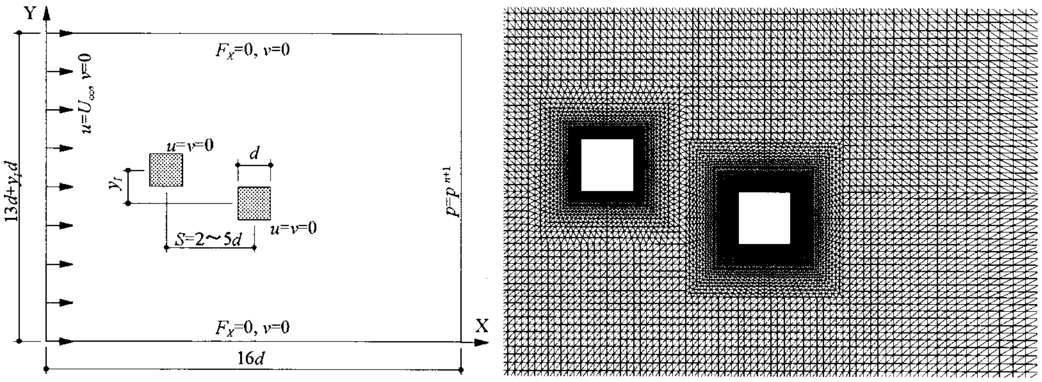

(a) model of two square columns **(b) mesh around columns (y_l=1.0)**

Figure 1. Case 1: 2D computations at low Reynolds numbers ($Re = 200$, 400 and 600).

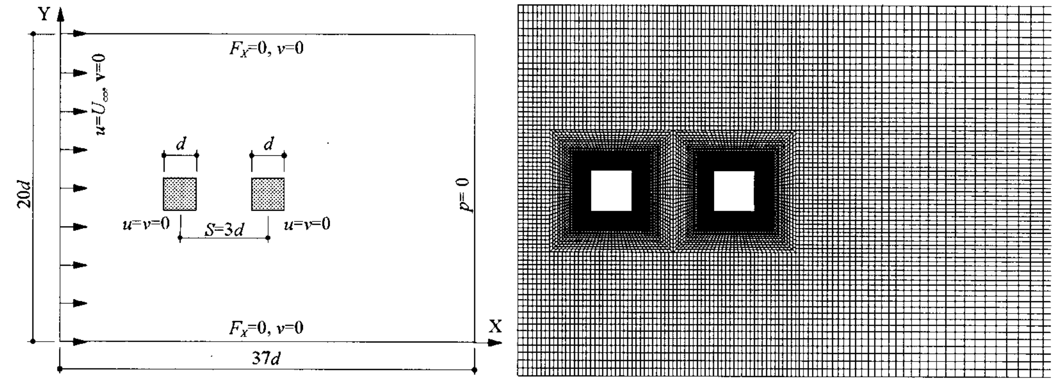

(a) model of two square columns (S=3d, y_l=0.0) (b) mesh around columns

Figure 2. Case 2: 2D computations at high Reynolds numbers ($Re = 10^3$, 10^4 and 10^5).

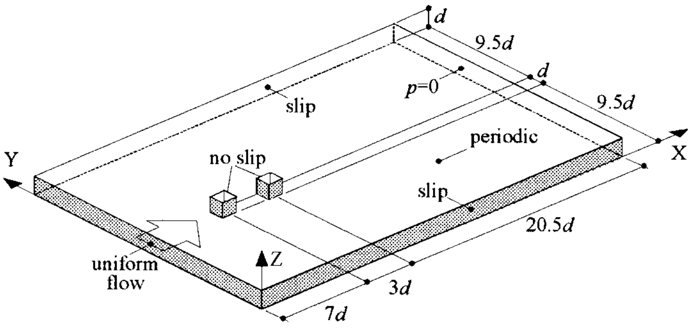

(a) model of square columns in tandem (S=3d, y_l=0.0)

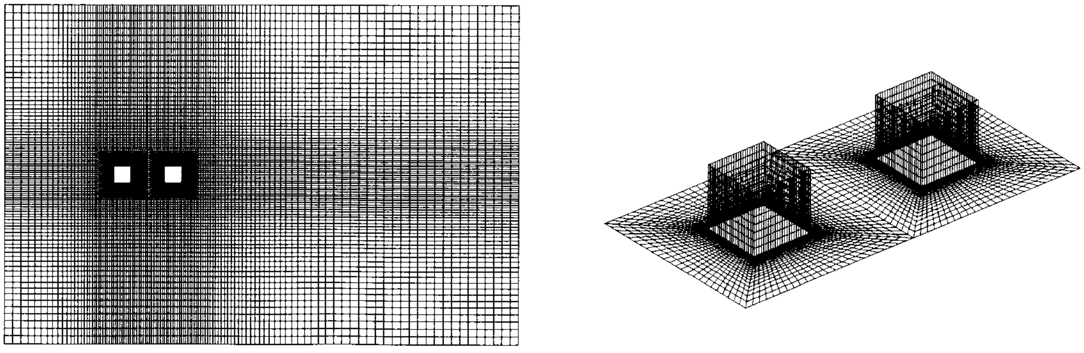

(b) sectional mesh on X-Y plane (c) mesh around columns

Figure 3. Case 3: 3D computations at $Re = 10^3$ and 10^4.

3. COMPUTATIONAL MODEL AND BOUNDARY CONDITIONS

The computational domains and the finite element meshes for 2D and 3D flows past the square columns in tandem are shown in Figures 1–3.

For the low Reynolds number, 2D computation (case 1), a linear triangular element was employed as shown in Figure 1. The dimension of the flow domain was set at $16d \times 14d$ (where d is the column width). The columns were placed with certain spacings in both the X- and Y-directions; the horizontal spacing, S, was set at $2d$, $3d$ and $5d$, and the relative vertical distance y_{I} $(=y/d)$ was changed from 0.0 to 1.0 by 0.5. The boundary conditions for Equation (4) were: $\boldsymbol{u} = U_\infty = 1$, $v = 0$ at the inlet, and $v = 0$, $F_x = 0$ at the top and bottom walls (where F_x is the friction force along the wall); natural boundary conditions were used at the exit. When using the FS method, the Dirichlet condition at the outlet boundary must be prescribed to solve the PPE. The condition in this case was obtained by the Shimura–Kawahara scheme [5]. The time-averaged pressure coefficient was computed for the leeward column and compared with the wind-tunnel results. Thus, the basic properties of the flow past square columns were investigated.

The finite element mesh using the quadrilateral element was used for the high Reynolds number 2D computation (case 2) as shown in Figure 2. The domain size of $37d \times 20d$ was chosen to keep the blockage factor as low as 5%. The boundary conditions were same as those of case 1 except that the pressure Dirichlet condition at the exit was set at $p = 0$. Consequently, the region in case 2 was made to be wider than that in case 1; so as not to be influenced by the prescribed condition $p = 0$. In order to clarify the dependence of aerodynamic coefficients on the Reynolds number in this case, the horizontal and relative vertical distances were fixed at $S = 3d$ and $y_{\mathrm{I}} = 0$, respectively.

In the study of the effect of 3D flow structure (case 3), the domain width was reduced from $37d$ (case 2) to $30.5d$ as shown in Figure 3(a), while the height of the region was set at $1d$ and divided into eight layers. The combination of these sizes was decided according to the memory restriction of the computer used. The spacings between the columns were the same as those in case 2: $\mathrm{S} = 3d$ and $y_{\mathrm{I}} = 0.0$, and each of the layers consisted of the same number of linear solid elements as shown in Figure 3(b) and (c). The boundary conditions around the XY-plane were the same as those of case 2, while the periodic condition was employed in the spanwise Z-direction. This means that the nodal pressure and velocities at $Z = 1d$ surface have the same values as those at the $Z = 0$ surface.

The total numerical parameters for each case are summarized in Table I.

The experimental pressure distributions around the leeward column were measured in the 2×2.5 m^2 wind-tunnel facility at Kawada Industries, Japan. The turbulence intensity of the test section is $< 0.3\%$, and the Reynolds number based on the uniform flow velocity and column width was 2.7×10^4.

4. NUMERICAL RESULTS

4.1. 2D simulation at low Reynolds numbers

The computational results at Reynolds numbers 200, 400 and 600, with various combi-

Table I. Model parameters

Parameter	Case 1	Case 2	Case 3
Reynolds numbers Re	200, 400, 600	10^3, 10^4, 10^5	10^3, 10^4
Number of grid points	13 211 ($y/d = 1.0$)	31 294	15 368 (2D) 12 2944 (3D)
Number of finite elements	25 856 ($y/d = 1.0$)	30 890	15 064 (2D) 12 0512 (3D)
Minimun element height δ	$0.007d$	$0.0014d$	$0.0035d$
Time increment Δt	0.0060 ($Re = 200, 400$) 0.0036 ($Re = 600$)	0.02 ($Re = 10^3, 10^4$) 0.01 ($Re = 10^5$)	0.02
Averaged time span $\bar{T}$	300–600 ($Re = 200$) 600–1200 ($Re = 400$) 180–900 ($Re = 600$)	200–1000	200–400 ($Re = 10^3$) 400–700 ($Re = 10^4$)

nations of vertical distance y_{I} and horizontal spacing S, were compared with the experimental values ($Re = 2.7 \times 10^4$) in terms of the qualitative flow properties.

Figure 4 shows the distribution of computed time-averaged pressure coefficients on the leeward column ($S = 3d$) along with the wind-tunnel results. The referential example of a single square post is shown in Figure 4(a). It can be seen from this figure that the differences between each calculation are very small for the single square column. When the results for the cylinders in tandem are shown graphically with respect to y_{I}, the differences are seen more clearly. In the case of $y_{\mathrm{I}} = 0.0$, calculated pressure distributions at $Re = 400$ and 600 are lower on the back and side surfaces, and higher on the front surface than those of experimental values. On the other hand, the computed results at $Re = 200$ agree well with the experimental values, as in Figure 4(b). A similar tendency is recognized in Figure 4(c), in which y_{I} is set at 0.5. When $y_{\mathrm{I}} = 1.0$ (Figure 4(d)), each computational result shows a good agreement with experimental values.

Figure 5 shows another set of results of calculations and experiments performed, where the horizontal spacing S was set at $2d$ and $5d$, and the vertical distance is fixed at $y_{\mathrm{I}} = 0.0$. The computed pressure distributions coalesce well with experimental values in each case examined. It is assumed, based on the results presented in Figures 4 and 5, that the flow pattern around the columns in tandem are stable for different Reynolds numbers, if the distance between the two columns is adequately wide or narrow.

For a better understanding of the above features, a comparison was made between $Re = 200$ and 400 by obtaining the instantaneous streamlines and pressure contours around the columns for the case of $S = 3d$ and $y_{\mathrm{I}} = 0.0$, which showed the most distinct differences between computational and experimental values. The results are presented in Figures 6 and 7. At $Re = 200$ (Figure 6), the flow is separated from the leading-edge corners of the windward column and passed along the imaginary lines of the upper and lower surfaces of the two columns. Contrary to this, the strong Kármán vortex arises behind the windward column at $Re = 400$ (Figure 7). The eddy flows down along the surface of leeward column, interacting with the vortex generated by the downstream column itself. According to the report by Takeuchi *et al.* [10], the flow patterns around the tandem columns with various horizontal arrangements have been classified into two types of states, as shown in Figure 8. The computational flow pattern at $Re = 200$ is close to the mode 'A', while the computed results at $Re = 400$ are similar to the mode 'B'. In their studies, when the flow condition shifted from 'A' to 'B', the horizontal spacing S was reported as being about $3d$; and both modes were observed at $S = 3d$. This can be seen in Figure 5, in which the computed results on $S = 2d$ (narrower case) and $S = 5d$ (wider case) have qualitatively agreed well with the experimental values. It may be considered that the experimental flow pattern in the present study for the case of $S = 3d$ was close to the state of the 'A' mode. As a result, the computed pressure coefficients at $Re = 200$ comparatively agreed with the wind-tunnel results.

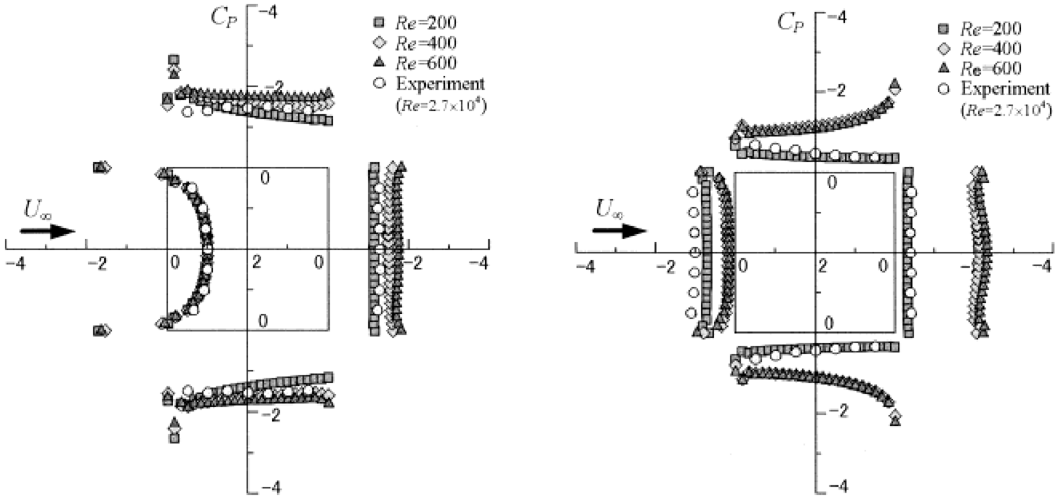

(a) single column

(b) leeward column (y_l=0.0)

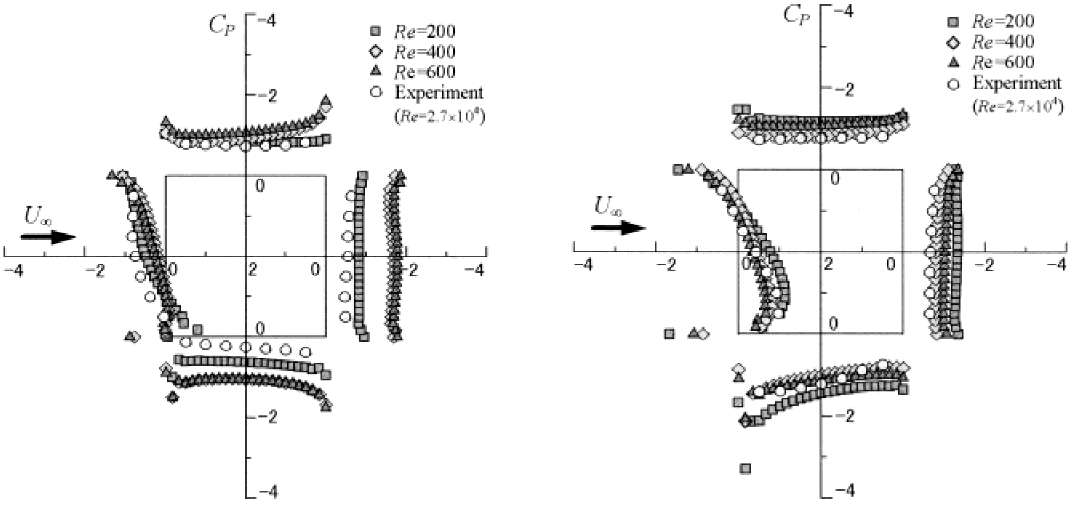

(c) leeward column (y_l=0.5)

(d) leeward column (y_l=1.0)

Figure 4. Time-averaged pressure coefficients at low Reynolds numbers ($S = 3d$).

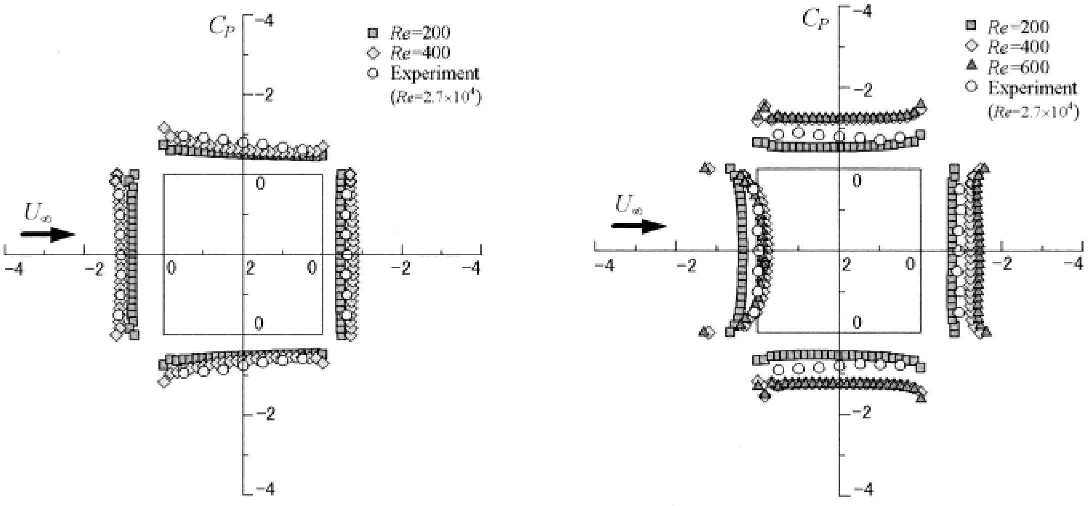

(a) leeward column (S=2d, y_I=0.0) (b) leeward column (S=5d, y_I=0.0)

Figure 5. Time-averaged pressure coefficients at low Reynolds numbers ($S = 2d$ and $5d$).

4.2. 2D simulation at high Reynolds numbers

To study the dependence of aerodynamic characteristics on Reynolds number, flow fields were computed in a higher Reynolds number range ($Re = 10^3 - 10^5$). These properties were compared with the wind-tunnel results, as in the previous section. The distances S and y_{I} were fixed at $S = 3d$ and $y_{\mathrm{I}} = 0.0$, which showed the most noticeable difference between the analysis and the experiment at low Reynolds numbers.

Figure 9 shows the drag coefficient C_{D} of the leeward column at Reynolds numbers $10^3 - 10^5$ and the prevailing frequency f_{L} (non-dimensional value) of the time history of lift force in combination with the results of $Re = 200 - 600$ and wind-tunnel tests. It is clear from Figure 9 that the C_{D} value (symbol □) is around 1.0 for Reynolds numbers $10^3 - 10^5$, while large variations of C_{D} are observed at Reynolds numbers below 10^3. It is assumed that a transient region exists in the low Reynolds number region where the flow pattern and the basic flow character change. Expressed in another way, the computed coefficients from 2D analyses scarcely changed at Reynolds numbers over a certain value. However, the computed C_{D} values were absolutely different from the experimental values; except the C_{D} at $Re = 200$. On the other hand, the prevailing frequency f_{L} (symbol ○) at $Re = 200$ was much greater than the experimental value. Thus, in 2D simulations of the flow past square columns in tandem, the numerical reproduction was hardly improved by the Reynolds numbers.

The pressure coefficients on the leeward column surfaces are shown in Figure 10 at Reynolds numbers 10^3, 10^4 and 10^5. It is noted that there is little change in the computed results at these Reynolds numbers, and basically they are similar to the characteristics at $Re = 400$ and 600 (Figure 4(b)). On the other hand, in comparison with the experimental values, the negative pressure values are smaller on the front surface, and larger on the back surface. Even on the side surfaces, the calculated pressure shows a reverse trend to the experimental values. To better understand this phenomenon, the instantaneous pressure contours at $Re = 10^4$ from non-dimensional time 1001 to 1004 are presented in Figure 11, together with the surface

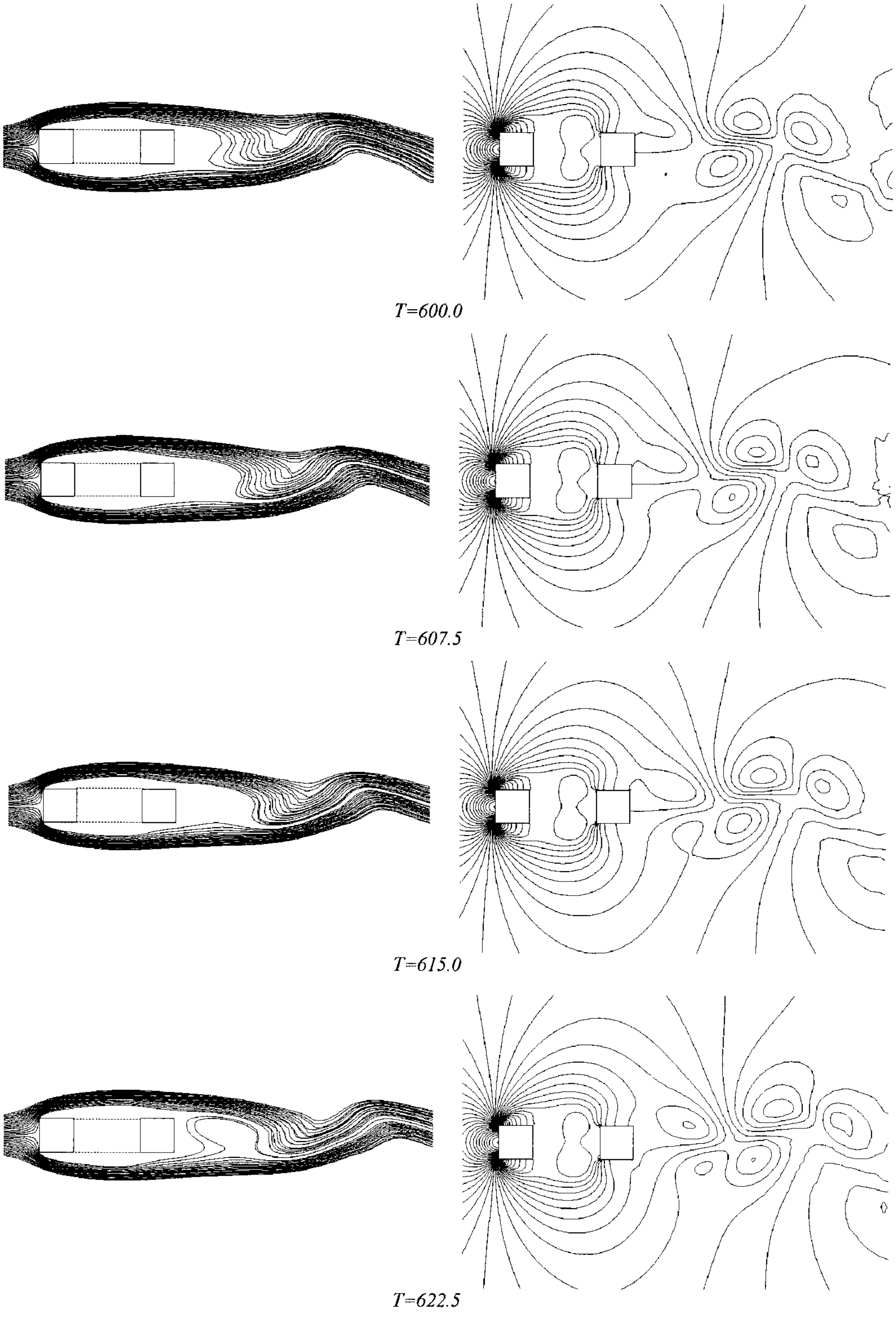

T=600.0

T=607.5

T=615.0

T=622.5

Figure 6. Instantaneous streamlines and pressure contours at $Re = 200$.

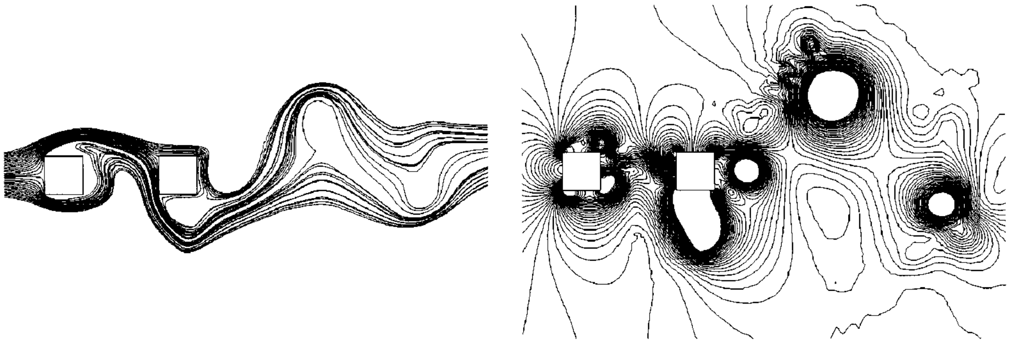

T=1500.0

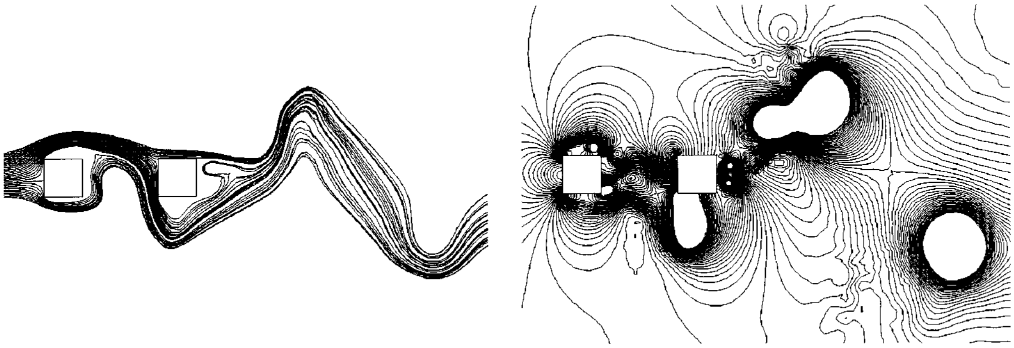

T=1507.5

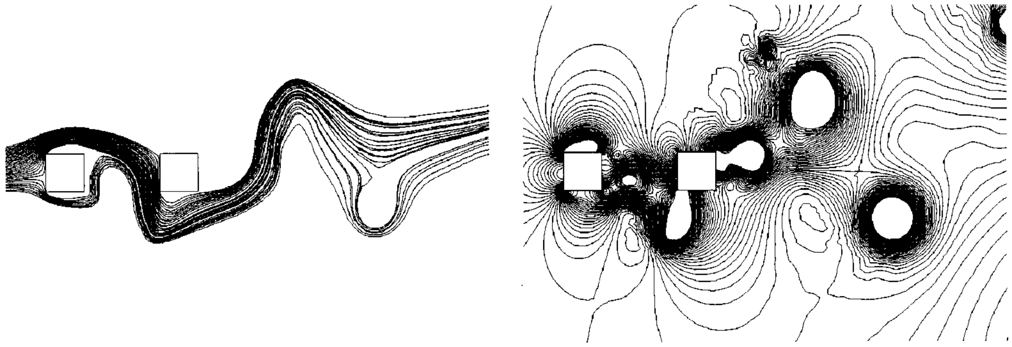

T=1515.0

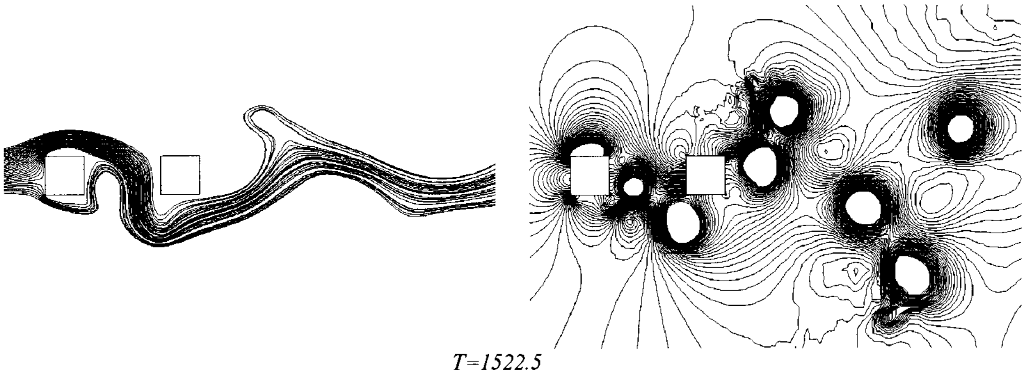

T=1522.5

Figure 7. Instantaneous streamlines and pressure contours at $Re = 400$.

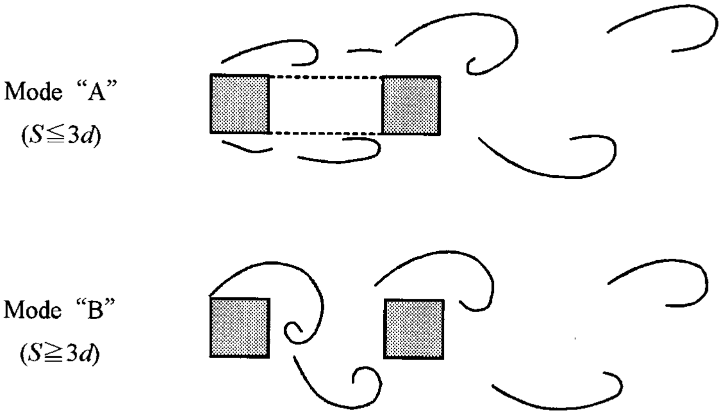

Figure 8. Two types of flow patterns around square columns in tandem [10].

pressure distributions. It can be seen in the pressure-contour diagrams that the vortices formed behind the windward column are unified with the separated bubbles of the leeward column, and then flows down along the side surface growing into a large eddy. It seems to be the flow pattern 'B' demonstrated in Figure 8. The surface pressure distribution shown in Figure 11 reveals that both negative and positive pressure fields act on the front surface of the leeward column; and this is the reason the average pressure coefficient on the front surface is near zero, as shown in Figure 10. While negative pressure may always exist on both side and back surfaces, the average pressures on each surface are negative and large, as presented in Figure 10.

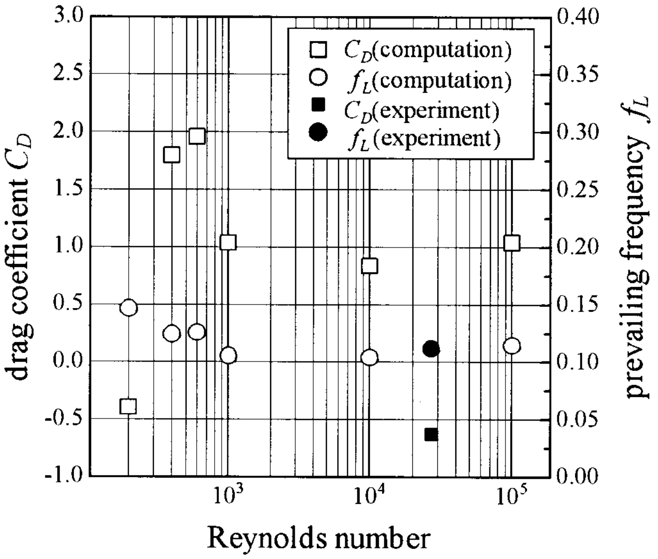

Figure 9. Drag coefficient and prevailing frequency of lift force.

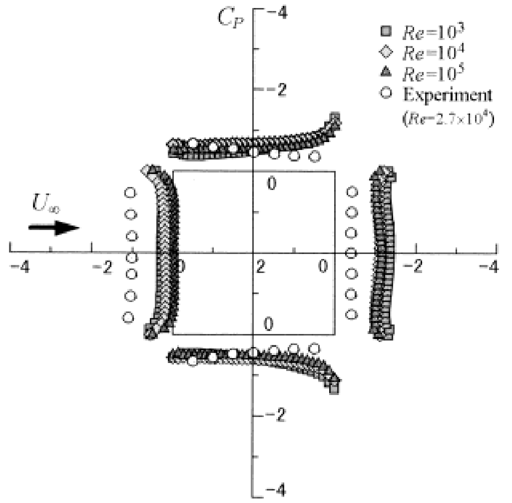

Figure 10. Time-averaged pressure coefficient on leeward column at high Reynolds numbers.

4.3. Effects of 3D computation

This section describes the 3D flow analysis based on the model shown in Figure 3, along with the analysis performed on the 2D model, in order to show the 3D effects. In order to study the Reynolds number effects, $Re = 10^3$ was used for non-dimensional times $T = 200-400$, and $Re = 10^4$ for $T = 400-700$. Figures 12 and 13 show the time histories of drag and lift coefficients in both 2D and 3D analyses. Figure 14 shows the behavior of midpoint velocity in the $Z = 0$ plane between the columns in which u_1, u_2 and u_3 are the velocity components in the X-, Y- and Z-directions, respectively.

It can be seen from Figures 12 and 13 at time $T = 200-400$ ($Re = 10^3$) that there is no significant difference in C_D variation between the 2D and 3D analyses, although 3D C_L variation demonstrates a relatively smaller fluctuation in amplitude than the 2D results. Judging from changes in midpoint axial velocities shown in Figure 14, it is concluded that the spanwise velocity u_3 starting at about time $T = 260$ reduced the magnitude of the lift fluctuation in the 3D analysis. However, the axial velocity u_2 shows a close correlation to the lift coefficient in 3D, and it should be a proof that there exists strong and periodic flow past the gap between two columns. This phenomenon has also been observed in 2D computations (Figures 7 and 11), so it can be said that the flow in the gap dominates the aerodynamic characteristics of the leeward column. The C_D value in 3D computations at $Re = 10^3$ showed a fluctuation centered around a positive (+) value because the flow past the gap was separating at the leading edge of the leeward column, as in the case of the well-known single square column. Contrary to this, in the wind-tunnel test, the flow between the two columns seemed to be nearly stagnating, resulting in the experimental drag coefficient of a negative (−) value at $C_D = -0.626$.

On the other hand, at $T = 400-700$ ($Re = 10^4$), the C_D and C_L variations with time in 3D computations behaved less violently compared with 2D or$Re = 10^3$ cases. In the 2D analysis, the C_D and C_L tended to be similar to the results of $Re = 10^3$, but with the 3D calculation, both the drag and lift fluctuations became smaller compared with those of $Re = 10^3$. Notably,

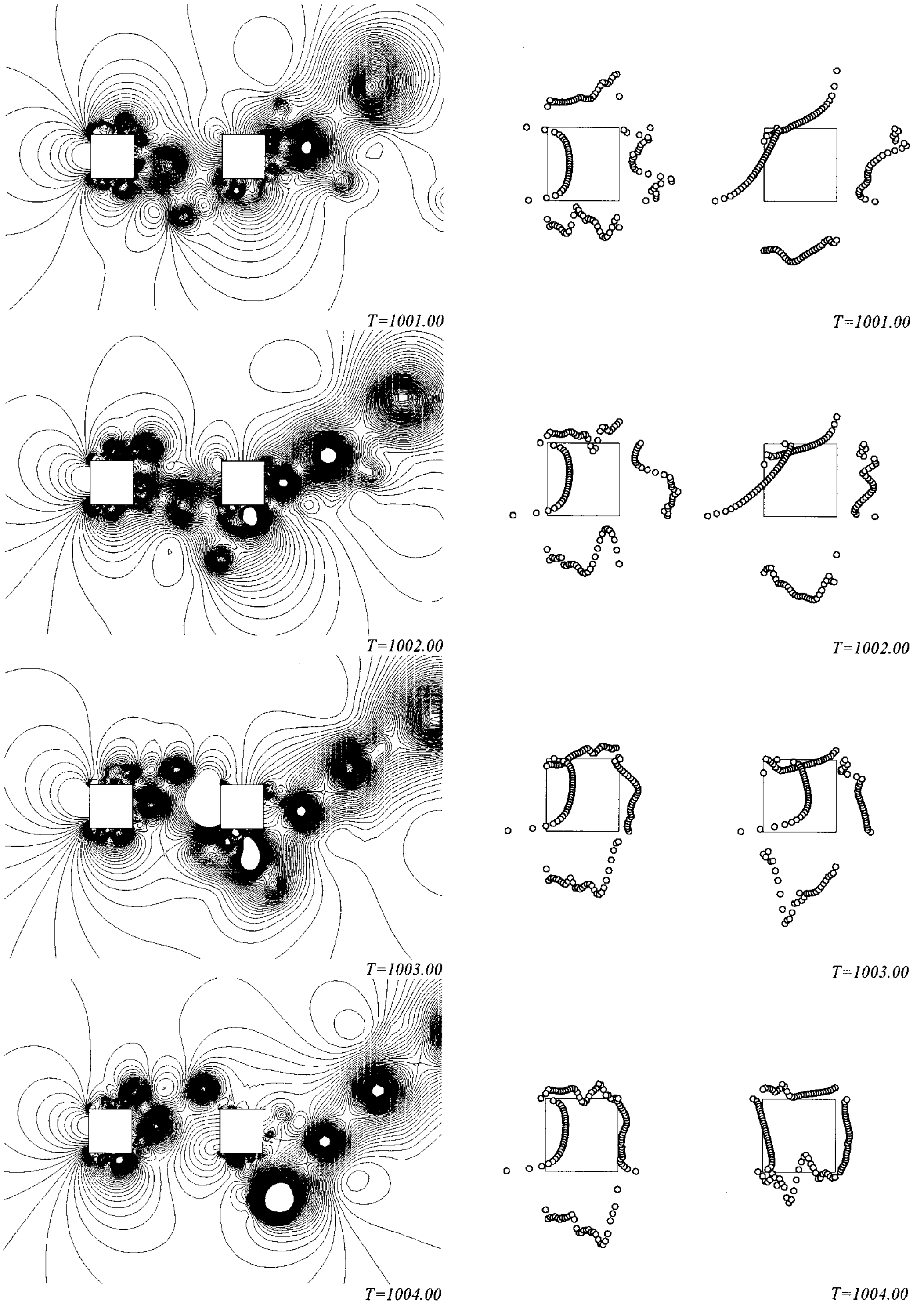

Figure 11. Instantaneous pressure contours and surface pressure distributions at $Re = 10^4$.

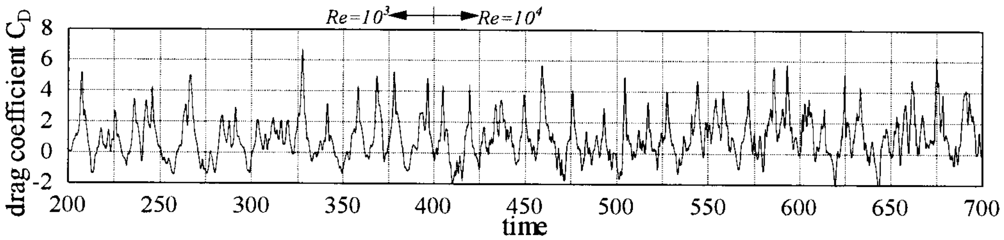

(a) 2D computation

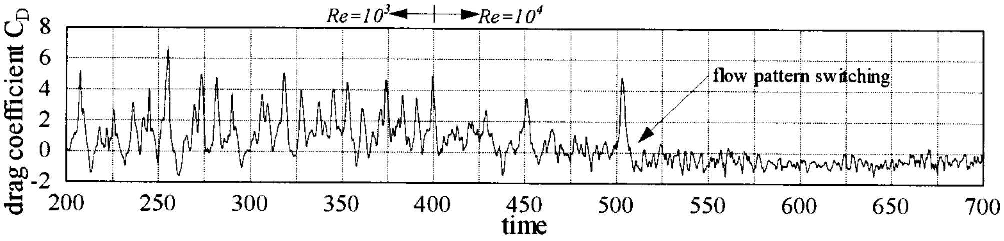

(b) 3D computation

Figure 12. Time history of lift coefficient C_D.

the drag showed the center of fluctuation shifting toward a negative (−) value. It is also found that the variation of axial velocity u_3, at $Re = 10^4$ and after $T = 400$, is even greater than that of $Re = 10^3$; and at the same time, the fluctuation of velocities u_1 and u_2 is gradually becoming irregular. It is significant that from the time shortly after $T = 500$, the characteristics of these coefficients and velocity components suddenly began to change, and it is presumed here that a mode switching from 'B' to 'A' occurred. The computed-average drag coefficient for $T = 400–700$, thus, became $C_D = -0.573$, which is close to the wind-tunnel result.

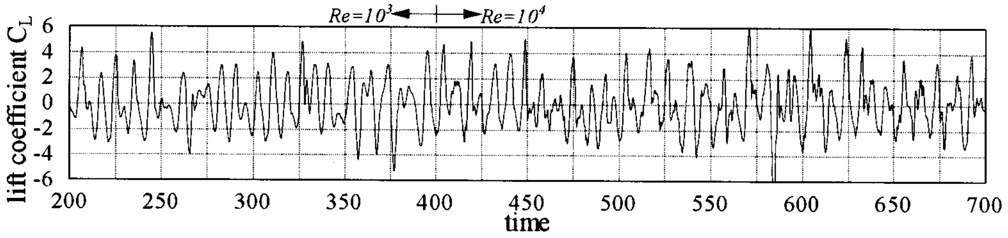

(a) 2D computation

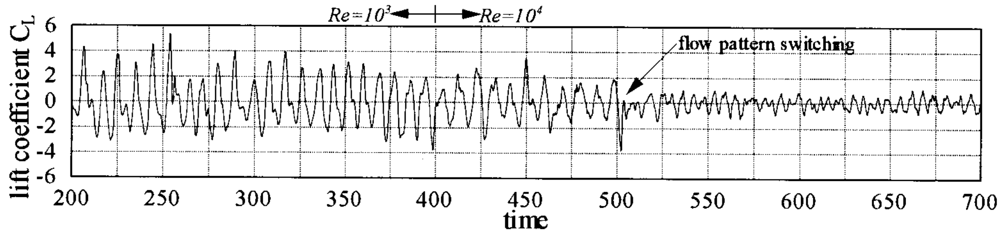

(b) 3D computation

Figure 13. Time history of lift coefficient C_L.

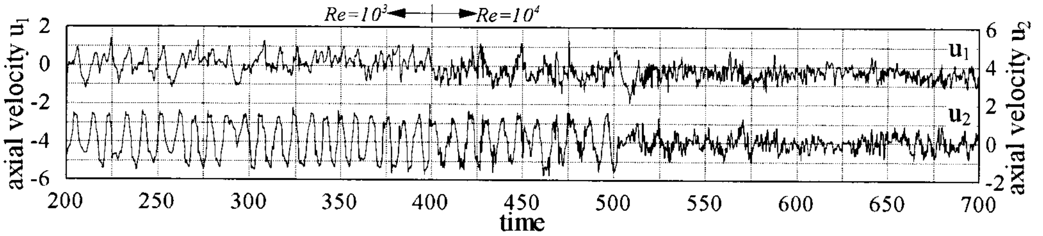

(a) axial velocities u_1 and u_2

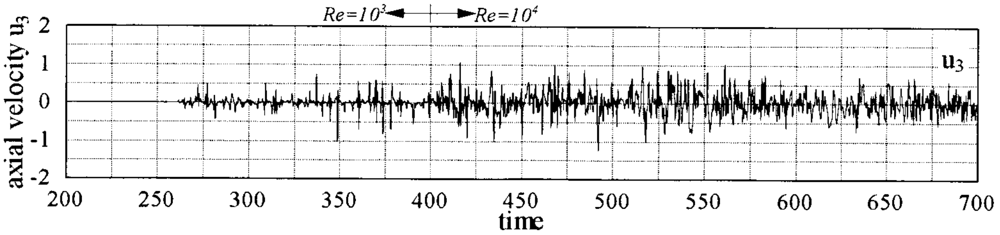

(b) axial velocity u_3

Figure 14. Time history of midpoint velocity in 3D computation.

The instantaneous 3D streamlines with pressure isosurfaces at $Re = 10^3$ and $Re = 10^4$ are compared, as shown in Figure 15. It can be seen from Figure 15(a) that the strong vortices retaining the 2D flow structure were formed behind each column. Consequently, the streamlines roll into the spaces behind each cylinder. On the other hand, according to the active spanwise diffusion, the strong vortex between the columns has dispersed, as in Figure 15(b). As a result in this case, the streamlines pass over the gap between two columns. This is the reason for the drag to shift to a negative (−) value, as seen in Figure 12(b), and it is considered to cause the changes in fluctuations of drag, lift and midpoint velocity. A comparison in the streamlines in the XY-plane before and after the mode switching at $Re = 10^4$ was made as shown in Figure 16. It is found that the flow pattern before the mode switching, Figure 16(a), is similar to that of the $Re = 400$ computational results (Figure 7), despite the difference in model configurations, namely 2D and 3D.

Figure 17 shows the distribution of average pressure coefficients in the 3D analyses. It was found that the computational results at $Re = 10^3$ are almost similar to the 2D values (e.g. Figure 4(b)), while the results at $Re = 10^4$ tend to be different from those of 2D cases; and the pressure distribution agrees well with the experimental result. This means that, in the case of $S = 3d$ and $y_{\mathrm{I}} = 0.0$, the reproduction of flow pattern plays an important role in improving consistency with the wind-tunnel result.

5. CONCLUSION

The results are summarized as follows

(1) The pressure coefficient distribution obtained from 2D analysis at low Reynolds numbers ($Re = 200$–600) agreed with the experimental values, as relative vertical distance y_{I} was increased. It appears to be a proof that the flow characteristics of the leeward column approach the properties of a single column with increasing y_{I}. Observations of the instanta-

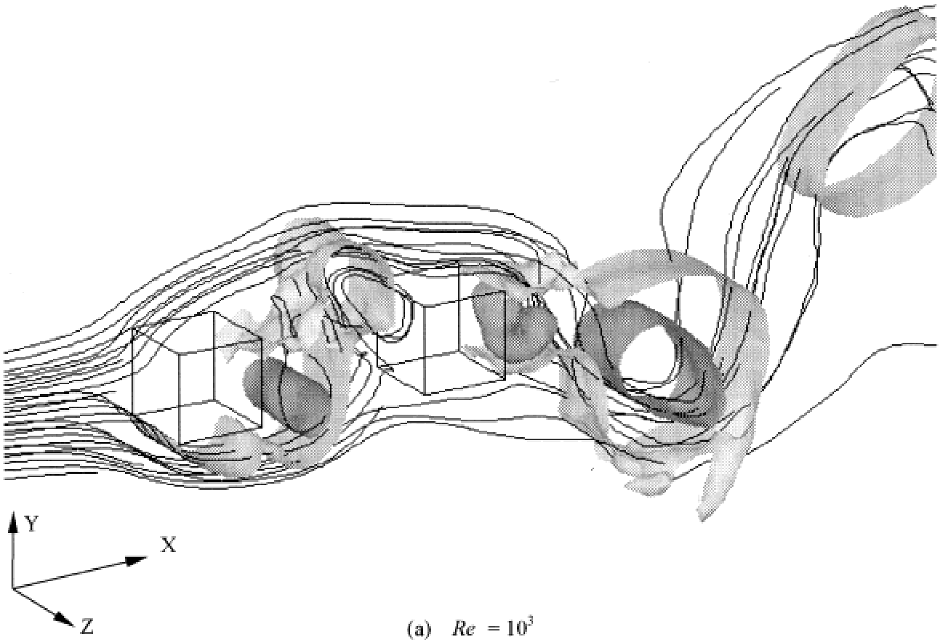

(a) $Re = 10^3$

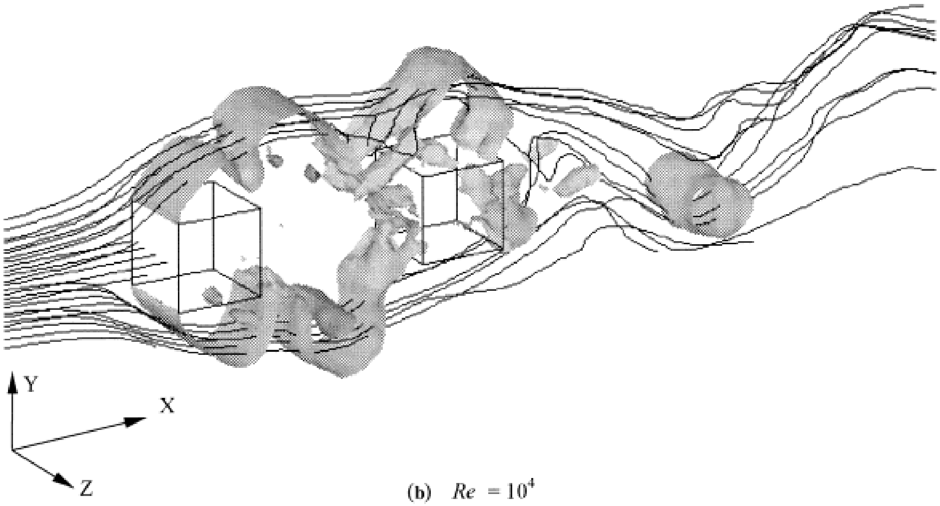

(b) $Re = 10^4$

Figure 15. Instantaneous streamlines with pressure isosurfaces at $Re = 10^3$ and 10^4.

neous streamlines and pressure contours generalized for $Re = 200$ and 400 revealed clear differences based on their flow patterns. The result at $Re = 200$ seems to have a flow pattern close to the actual phenomenon; thus, the pressure coefficient distribution at $Re = 200$ agrees well with the experimental value.

(2) The drag coefficient and prevailing frequency of the lift force evaluated from a 2D computation at high Reynolds numbers ($Re = 10^3$–10^5) scarcely changed with the Reynolds numbers, and then the time-averaged distribution of surface pressure coefficients showed a different feature in comparison with the experimental results. Observing the sequential results of surface pressure distributions at $Re = 10^4$, the strong vortices passed through the gap

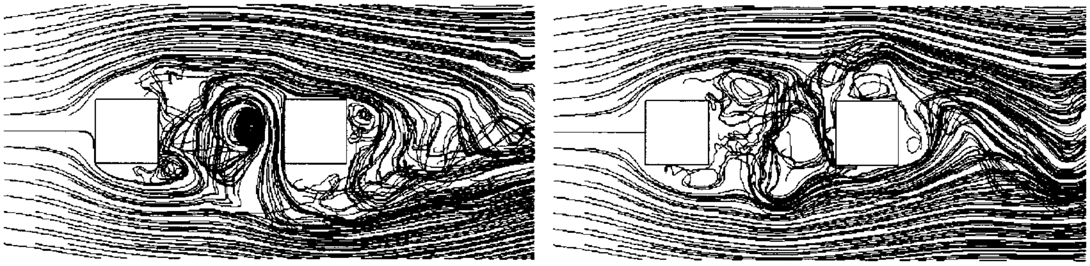
(a) before mode switching (b) after mode switching

Figure 16. Instantaneous 3D streamlines in the XY-plane before and after mode switching.

between the columns, and there appeared no distinct difference in flow pattern compared with the streamline at $Re = 400$. These results suggest that the Reynolds number is not a dominant parameter reflecting the actual phenomena; at least in the 2D computation of flow around columns in tandem arrangement ($S = 3d$ and $y_I = 0.0$).

(3) From the results of the 3D computation at $Re = 10^3$ and 10^4, the fluctuations of drag and lift amplitude decreased with the development of the spanwise flow. The 3D flow structure at $Re = 10^3$, which basically has a strong 2D nature, was weakened when the Reynolds number was increased to 10^4. This is because the active spanwise diffusion took place with growing axial velocity u_3. As a result, in the case of $Re = 10^4$, the drag coefficient shifted to the negative ($-$) side, and the fluctuations of both drag and lift coefficients of the leeward column were clearly decreased. The computed pressure coefficient agreed well with the experimental result. Thus, Reynolds numbers played an important roll when the analysis was performed with 3D models.

These results indicate meaningful values of 3D computations in studying the flow characteristics around structures in tandem, although it is difficult to say that the 3D flow structure has been clearly captured in this study. However, it can be considered that the 2D computation is also useful in the calculation of average flow characteristics when the structures are set at sufficiently wider (or narrower) spacings.

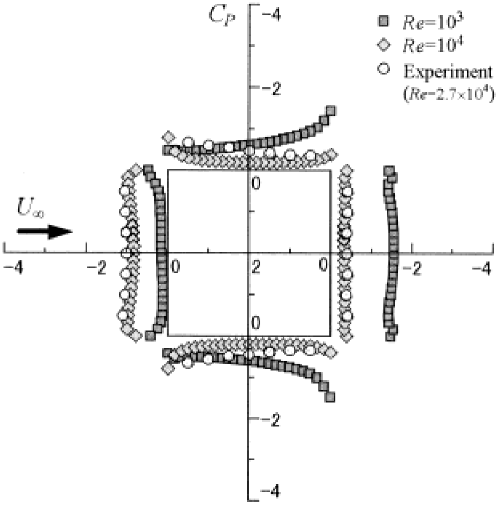

Figure 17. Time-averaged pressure coefficient in 3D computation.

The square columns in tandem handled here had complicated flow structures. Such computational models presented difficult tasks to reproduce the actual flow condition in numerical simulation. Thus, it is necessary to perform computations with Reynolds numbers equivalent to those in tests, giving considerations to the 3D flow structure. It will be necessary in future to accumulate numerical examples of other structures and their spatial arrangements when the application of CFD to practical design operations is considered.

REFERENCES

1. K. Edamoto, M. Yoneda and M. Kawahara, 'Finite element analysis for wind forces on tandem circular cylinders when its stationary and forced vibration state', *J. Struct. Eng. A*, **41**, 369–376 (1995).
2. H. Kawai and T. Kanasugi, 'Numerical simulation on flow around two circular cylinders', *J. Wind Eng.*, **63**, 51–52 (1995).
3. Y. Ouwa, F. Sakao and Y. Matsuoka, 'Numerical analysis of unsteady flows around two square cylinders set tandem between two parallel walls', *Trans. JSME B*, **55**, 1513–1517 (1989).
4. M. Hayashi, K. Hatanaka and M. Kawahara, 'Lagrangian finite element method for free surface Navier–Stokes flow using fractional step method', *Int. j. numer. methods fluids*, **13**, 805–840 (1991).
5. M. Shimura and M. Kawahara, 'Two-dimensional finite element flow analysis using the velocity correction method', *Proc. JSCE*, **398**, 51–59 (1990).
6. A. Maruoka, S. Ohta, H. Hirano and M. Kawahara, 'An incompressible viscous flow analysis by finite element method using equal-order interpolation', *J. Struct. Eng. A*, **43**, 369–376 (1997).
7. P.M. Gresho, S.T. Chan, R.L. Lee and C.D. Upson, 'A modified finite element method for the solving the time-dependent incompressible Navier–Stokes equations, part 1 and 2', *Int. j. numer. methods fluids*, **4**, 557–598, 619–640 (1984).
8. P.M. Gresho and S.T. Chan, 'Semi-consistent mass matrix techniques for solving the incompressible Navier–Stokes equations', Lawrence Livermore National Laboratory, *Preprint UCRL-99503* (1988).
9. V. Selmin, J. Donea and L. Quartapelle, 'Finite element methods for non-linear advection', *Comput. Methods Appl. Mech. Eng.*, **52**, 817–845 (1985).
10. T. Takeuchi, M. Matsumoto and N. Shiraishi, 'On wind-induced vibrations of tandem columns for bridge tower', *J. Wind Eng.*, **41**, 41–42 (1989).